


Communication

A Universal Phase Error Analysis for Optical Frequency Tuning Lasers Utilized in Fiber Sensing with OFDR

Zheyi Yao ^{1,2} , Zhewen Yuan ¹, Guohua Gu ¹, Qian Chen ¹ and Xiubao Sui ^{1,*}¹ School of Electronic Engineering and Optoelectronic Technology, Nanjing University of Science and Technology, Nanjing 210094, China² The Jiangsu Key Laboratory of Spectral Imaging & Intelligent Sense, Nanjing 210094, China* Correspondence: sxb@njust.edu.cn

Abstract: As optical fiber sensing has attracted increasing attention due to its advantages such as high accuracy, low costs, and stability, its optical source judgment has become an attractive issue by which to characterize its performance. Optical frequency-domain reflectometry (OFDR) has been demonstrated as a means of the fiber identification (ID) of optical fibers; however, the linearity of the optical frequency tuning rate determines both the spatial resolution and detection range. In this paper, the results from various simulations and experiments show that the phase error from the initial frequency and tuning rate can affect the performance of the OFDR system, which directs the future improvement direction of fiber sensing based on such technology.

Keywords: optical frequency-domain reflectometry; tunable semiconductor laser; fiber sensor



Citation: Yao, Z.; Yuan, Z.; Gu, G.; Chen, Q.; Sui, X. A Universal Phase Error Analysis for Optical Frequency Tuning Lasers Utilized in Fiber Sensing with OFDR. *Photonics* **2022**, *9*, 922. <https://doi.org/10.3390/photonics9120922>

Received: 26 October 2022

Accepted: 27 November 2022

Published: 30 November 2022

Publisher's Note: MDPI stays neutral with regard to jurisdictional claims in published maps and institutional affiliations.



Copyright: © 2022 by the authors. Licensee MDPI, Basel, Switzerland. This article is an open access article distributed under the terms and conditions of the Creative Commons Attribution (CC BY) license (<https://creativecommons.org/licenses/by/4.0/>).

1. Introduction

Benefiting from low costs, a high data rate, and relative immunity to electromagnetic interference, optical fibers have been broadly applied in the telecommunication and sensing fields and are an ideal means for image transmission [1,2]. In earlier designs, since a laser source is utilized to emit the original light, it plays a fundamental role in determining the accuracy of the whole system. Unlike optical time-domain reflectometry (OTDR), optical frequency-domain reflectometry (OFDR) works in the frequency domain using continuous wave (CW) light sources, which enable higher signal-to-noise ratios [3]. Moreover, because of the advantages in the light frequency-domain techniques, including their sensitive measuring ability, high spatial resolution, and low-power consumption, there are some applications for these frequency-swept lasers: OFDR-based distributed sensing [4]; spectroscopy [5]; the optical physical unclonable function (PUF) [6] or fiber ID [7]; fiber sensors [8,9]; and the frequency-modulated continuous-wave (FMCW) LiDAR [10]. To meet the highly linear and coherent light source required in the above applications, various laser control methods and designs [11–13] have been proposed. Additionally, there are several principles or theories that have been investigated as means of improving the performance, such as the injection locking [14] design by enhancing the modulation bandwidth, integrated structures [15,16] on a single CMOS-compatible chip with multi-channel sensors, parallel coherent ranging by microcombs [17], and polarization control module analysis to suppress the wave-mixing influence [18]. In addition, there are some models that have been proposed to describe the laser's performances as well, including the noise, bandwidth, and polarization [19,20]. Furthermore, only when the precise laser frequency module has been built can the optical system achieve accurate measurements [21].

Considering that the tuning laser applied in the frequency-domain area can generally be categorized as two mechanisms—wavelength modulation and frequency modulation—both of them complete the control by changing the geometry size of the resonator [13,22]. It is no doubt that the former technique suffers from an inverse relation between the frequency and wavelength. In comparison, the latter is utilized to modulate the optical frequency

directly, then such a light source can be toned linearly in the frequency domain without an extra transform function. Distributed feedback semiconductor lasers (DFB-SCLs) have been broadly implemented in the telecommunication and sensing fields due to their lightweight design, solid state, simple control, and low power consumption [23]. They are convenient for generating the required highly linear frequency-sweeping optical source by modulating the junction current [24]. Importantly, both the optical frequency linearity and initial frequency [6] of these lasers determine the sensing resolution and distance, and such properties are from the intrinsic structure and material of the laser itself [25].

In this study, in order to analyze the issues influencing optical frequency tuning progress, an analytical model was established to determine the optical frequency-domain measuring system. By taking both the frequency-swept velocity error and initial frequency variance into account, the module was able to quantify the frequency-domain performance. Furthermore, a simulation and various experiments based on DFB-SCLs were completed; both verified the proposed module accurately, promising further improvements to this technology.

2. Theory and Implementation

Taking the DFB-SCL laser as an example, the general optical frequency modulating system is depicted in Figure 1. A DFB-SCL provides the optical source and is generated by a time-varying current curve from the driving circuit (DRI) that is controlled by the control loop (CL), and the Mach–Zehnder interferometer (MZI) is utilized to monitor the optical linearity converted by a balanced photodetector (BPD). Additionally, the optical coupler (CPL) is utilized to divide the optical source into two parts: controlling and measuring. As introduced in previous works [11,26], a small MZI delay, τ_d , would result in a flat phase and frequency response. During the controlling period, T_C , the SCL optical frequency, $f_{opt}(t)$, can be expressed as

$$f_{opt}(t) = f_0 + v_0t + e(t) \tag{1}$$

where f_0 is the initial optical frequency (IOF); v_0 is the laser frequency slope over time, which is also termed the frequency-sweep velocity (FSV); $e(t)$ is the corresponding frequency error in the laser frequency sweeping; and t is the time. To determine the relations in the $e(t)$ part, it is treated as the tuning frequency, and the initial frequency-varying errors are

$$e(t) = \Delta v(t) + \Delta f_0(t) \tag{2}$$

where $\Delta v(t)$ and $\Delta f_0(t)$ are the laser FSV and IOF errors over time, respectively.

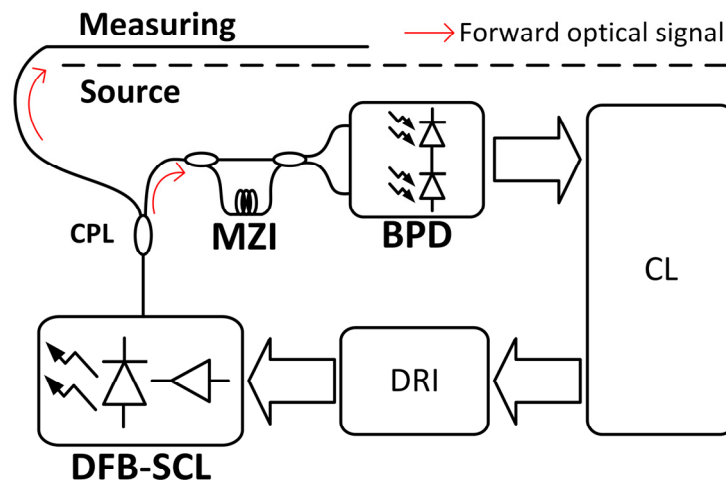


Figure 1. Schematic of the general laser tuning measuring system. DFB-SCL, distributed feedback semiconductor laser; CPL, optical couplers; MZI, Mach–Zehnder interferometer providing the time delay; BPD, balanced photodetector; CL, laser frequency-sweep control loop; DRI, laser driving circuit.

Moreover, the MZI phase, $\phi_{MZI}(t)$, is the phase difference between its two arms [27,28], which can be expressed as

$$\begin{aligned} \phi_{MZI}(t) &= \int_{t-\tau_d}^t f_{opt}(\tau) d\tau \\ &= 2\pi \left(v_0 \tau_d t + f_0 \tau_d - \frac{v_0 \tau_d^2}{2} + E(t) - E(t - \tau_d) \right) \\ &= 2\pi (v_0 \tau_d t) + 2\pi f_0 \tau_d - \pi v_0 \tau_d^2 + 2\pi [E(t) - E(t - \tau_d)] \end{aligned} \tag{3}$$

where τ_d is the MZI time delay and $E(t)$ is the integral of $e(t)$, or $E(t) = \int_0^t e(\tau) d\tau$.

For a given system, since the f_0 , τ_d , and v_0 are constant, to analyze the elements that influence the measuring accuracy, the remaining parts require quantitative investigation.

Considering that the phase differential of MZI is resolved and can be described as

$$\begin{aligned} f_{MZI}(t) &= \frac{1}{2\pi} \frac{d}{dt} \phi_{MZI}(t) \\ &= v_0 \tau_d + \frac{d}{dt} E(t) \\ &= v_0 \tau_d + e(t) \end{aligned} \tag{4}$$

then, the remaining part, $e(t)$, is the optical frequency error that results in the poor performance. Furthermore, if τ_d is relatively small enough or close to 0, the relation can be expressed as

$$\begin{aligned} e(t) &= \frac{d}{dt} E(t) \\ &= \lim_{\tau_d \rightarrow 0} \frac{E(t) - E(t - \tau_d)}{\tau_d} \\ &= \lim_{\tau_d \rightarrow 0} e_{\tau_d}(t) \end{aligned} \tag{5}$$

where $e_{\tau_d}(t)$ is defined as the approaching frequency error.

For the bandwidth-limited laser, with the control period, T_C , its relation between bandwidth, B , and frequency-sweep velocity, $v(t)$, can be expressed as

$$B = \int_0^{T_C} v(t) dt \tag{6}$$

As for the linear frequency tuning laser, $v(t) = v_0$, which means $B = v_0 T_C$. From the above equations, the conclusion that the frequency of the MZI signal is independent of the time delay τ_d can be reached. In reality, it is a difficult choice to set the MZI delay for a bandwidth-limited laser because a longer delay results in a lower tuning optical frequency-swept velocity that can easily be captured with greater errors in $e(t)$ than the shorter one.

For practical situations, since it is difficult to generate the ideally linear optical frequency tuning laser source, assume that both the tuning velocity error, $\Delta v(t)$, and initial frequency oscillation, $\Delta f_0(t)$, follow Gaussian distributions:

$$\Delta v(t) \sim \mathcal{N}(0, \sigma_v) \tag{7}$$

$$\Delta f_0(t) \sim \mathcal{N}(0, \sigma_{f_0}) \tag{8}$$

where σ_v and σ_{f_0} are the standard deviations for the tuning velocity error and initial frequency oscillations, respectively.

If the two components in the laser frequency tuning error, $e(t)$, are independent of each other, they are supposed to also follow a Gaussian distribution [29] and can be expressed as

$$e(t) \sim \mathcal{N}\left(0, \sqrt{\sigma_v^2 + \sigma_{f_0}^2}\right) \tag{9}$$

From Equation (5), $e_{\tau_d}(t)$ is also supposed to follow a Gaussian distribution when τ_d is much greater than unity:

$$e_{\tau_d}(t) \sim \mathcal{N}\left(0, \sqrt{\frac{\sigma_v^2 + \sigma_{f_0}^2}{\tau_d f_s}}\right) \tag{10}$$

where f_s is the system sampling rate, and $\sqrt{\tau_d f_s}$ represents the quantified number of the statistics.

Furthermore, for the random distribution data that have a mean of 0 [30], the greater the integrating time, the fewer the absolute errors.

3. Simulations and Experiments

To verify the influence caused by the τ_d , the following parameters shown in Table 1 are set to complete the simulations.

Table 1. Simulation parameters.

Symbols	Values
f_s	125 MSamples/second
τ_d	16 ns, 160 ns, 320 ns
T_C	100 μ s
f_0	193 THz
v_0	125 GHz/ms
σ_v	10^5
σ_{f_0}	10^5

From Equation (5), it can be concluded that only when the time delay, τ_d , is tiny enough can the precise mathematic model, $e(t)$, be captured. However, as introduced above, it is difficult to choose between the time delay and accuracy of the MZI frequency; even though a lower time delay results in the more accurate tuning rate, a greater time delay leads to fewer standard deviations, termed σ_{sim} . To quantify the performance of the results, the simulation error, $err_{\sigma}(\tau_d)$, rate is defined as

$$err_{\sigma}(\tau_d) = \frac{\left| \sigma_{sim} - \sqrt{\frac{\sigma_v^2 + \sigma_{f_0}^2}{\tau_d f_s}} \right|}{\sqrt{\frac{\sigma_v^2 + \sigma_{f_0}^2}{\tau_d f_s}}} \tag{11}$$

Figure 2 illustrates the simulations with various time delays, τ_d . To express the difference in the frequency domain, Figure 2(a1–c1) shows the fast Fourier transform (FFT) results, in which the frequency of the maximum value is supposed to be 125 GHz/ms. Then, there are the two periods of the MZI signal in the time domains shown in Figure 2(a2–c2), in which the amplitude is set as a united value to simplify the phase part of the tuning frequency laser, and it is clear that the time accuracy decreases when the time delay increases, which is caused by the limited system sampling rate. Figure 2(a3–c3) depicts the short-time FFT (STFFT) results for the various simulations with noise, in which the Hamming window is selected to complete the FFT calculations. As for the statistics of the simulations, the results are shown in Figure 2(a4–c4), and the detailed values for the simulation of the approaching frequency error are illustrated in Table 2.

As mentioned in the theory section, the error rate between the theory and simulation standard deviations increases, but the absolute value of the simulation mean decreases with increases in the time delay.

To empirically evaluate the accuracy of the proposed phase error model of the SCL and the optimized algorithm for verifying the relations of the fiber subsets, experimental testing with a semiconductor laser (Eblana EP1550-NLW-B, 1550 nm) was carried out using the parameters shown in Table 3, and with a 125 Msamples/second system sampling rate.

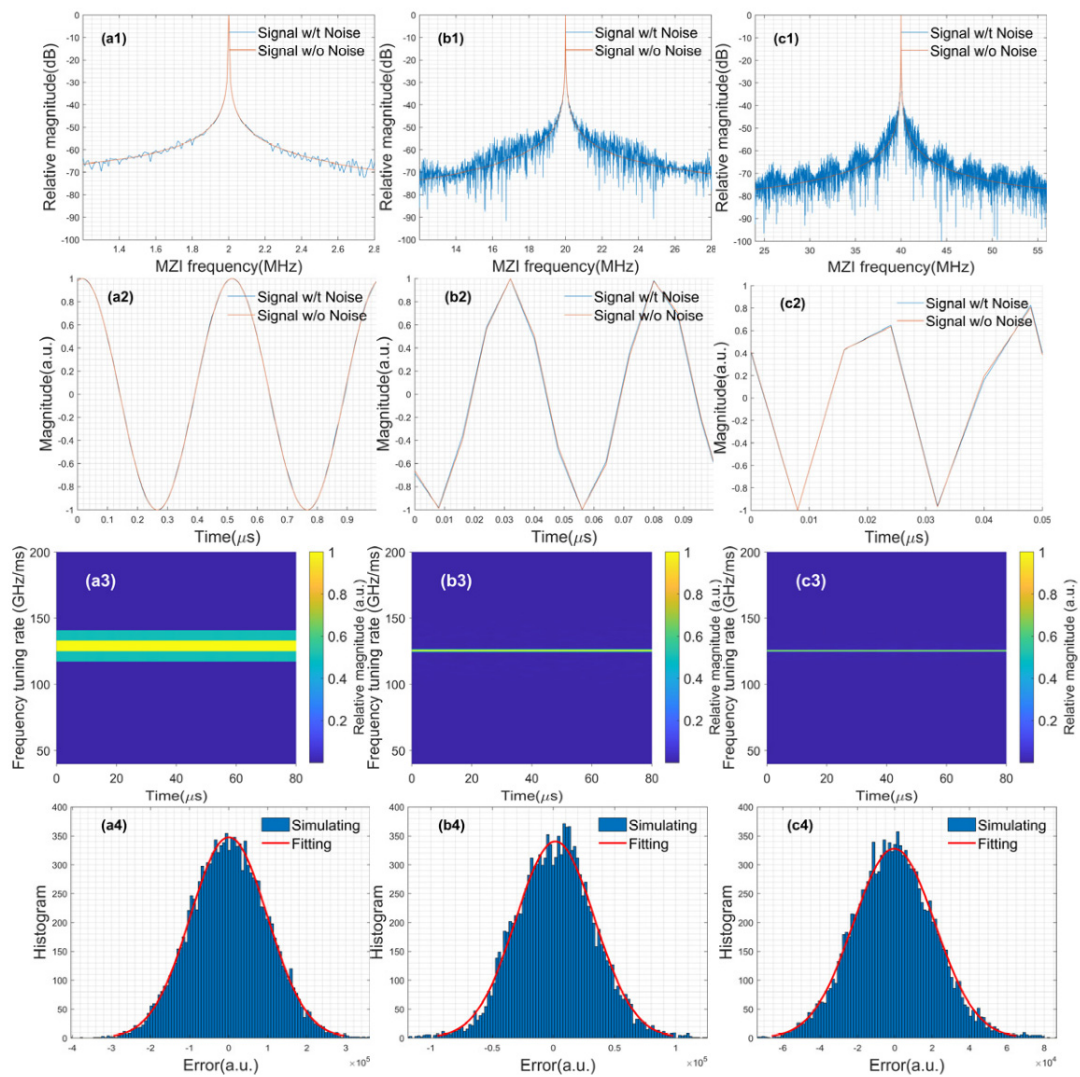


Figure 2. Simulation results with the same conditions but various time delays. (a1–a4) Time delay, 16 ns; (b1–b4) time delay, 160 ns; (c1–c4) time delay, 320 ns; (a1–c1) FFT results of the MZI signals in the frequency domain; (a2–c2) results of the MZI signals in the time domain with two periods; (a3–c3) short-time FFT (STFFT) results for the MZI signals with the Hamming window; (a4–c4) histograms for the approaching frequency error.

Table 2. Simulation statistics.

τ_d	Theory σ	Simulation σ	Simulation Mean	Error Rate (%)
16 ns	10,000	99,616	1031	0.39
160 ns	31,623	32,877	−632	3.82
320 ns	22,361	21,495	−482	5.98

Table 3. Experimental setup and parameters for various time delay.

Components	Name or Values
$\nu_0 \tau_d$	6.25 MHz
τ_d	10 ns, 100 ns, 250 ns
T_C	50 μ s, 500 μ s, 1000 μ s

A comparison between the various time delays, including 10 ns, 100 ns, and 250 ns, in which the MZI frequency was set to 6.25 MHz and 12.5 MHz, is depicted in Figure 3.

Similar to the simulation results, as the time delay increased, the distortions in the tuning laser increased simultaneously; the FFT results from the MZI signals in the region of interest (ROI) are shown in Figure 3(a1–c1). As mentioned in the theory section, the tuning rate was limited by both the time delay and the laser tuning bandwidth. Compared with Figure 3(a3–c3), there was a roughly constant value that is the product between the tuning rate, v_0 , and the control period, T_C , which is supposed to be the optical bandwidth of the laser.

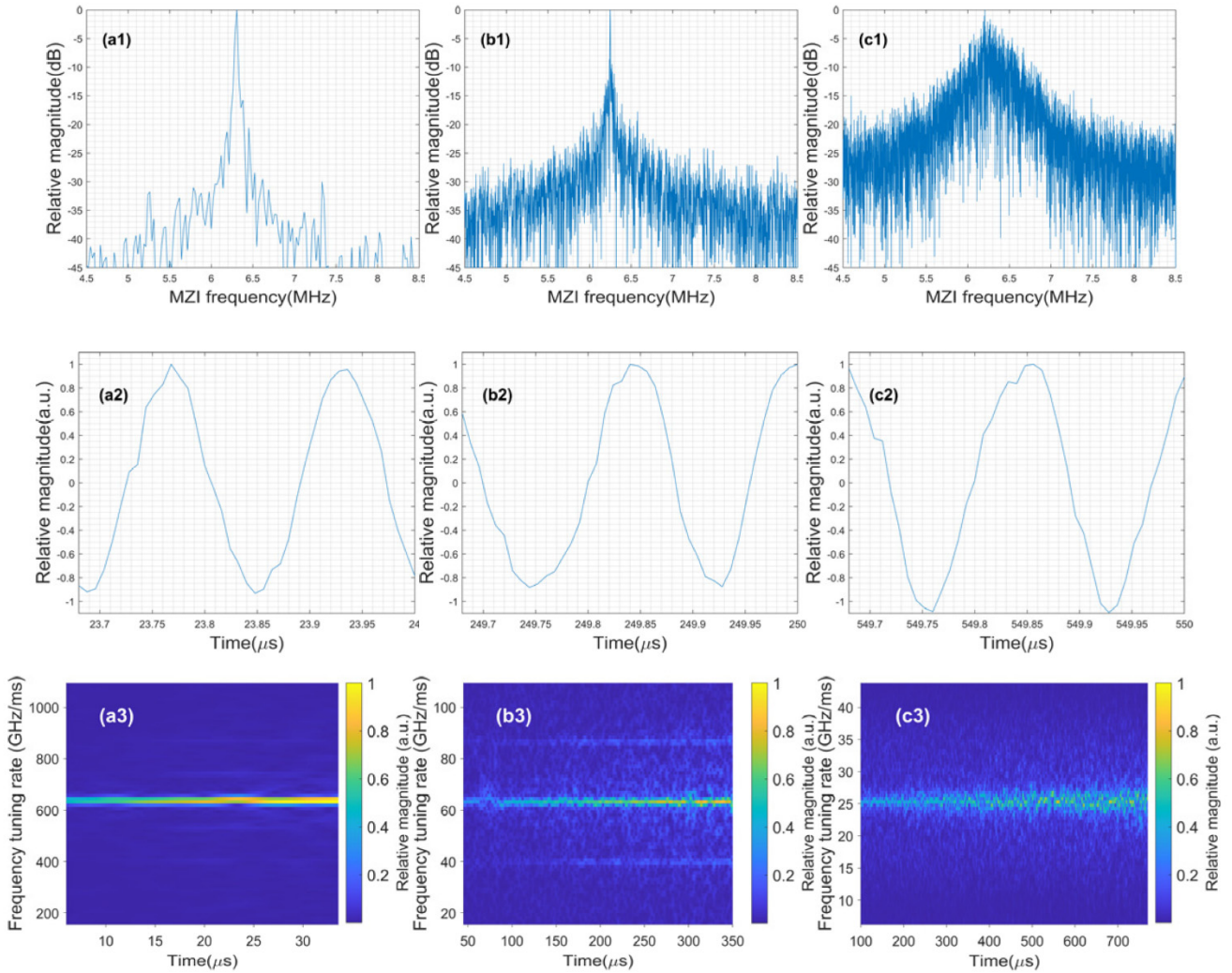


Figure 3. Experimental results with the various time delays and optical frequency tuning rates. (a1–a3) Time delay, 10 ns; (b1–b3) time delay, 100 ns; (c1–c3) time delay, 250 ns; (a1–c1) FFT results of the MZI signals in the region of interest (ROI) in the frequency domain; (a2–c2) results of the MZI signals in the time domain with two periods; (a3–c3) short-time FFT (STFFT) results of the MZI signals with the Hamming window.

Furthermore, to analyze the influence of the tuning rate at the same time delay, we set up experiments with the parameters shown in Table 4. Since the time delays utilized in the experiments were the same, the phase error from the τ_d could be treated equally. The results are shown in Figure 4.

From the experiments mentioned above, it was clear that the phase error of the optical tuning source increased with increases in the frequency tuning velocity, as the sideband noise shown in Figure 4(a1–c1) and Figure 3(b3) illustrate. However, both the system sampling rate and the optical bandwidth limited the accuracy of the sensing system that

was based on the optical continuous wave, even though there were some extra approaches utilized to minimize such influence to improve the stability and application areas.

Table 4. Experimental setup and parameters for various tuning rates.

Components	Name or Values
$v_0\tau_d$	10.42 MHz, 12.5 MHz, 15.63 MHz
τ_d	100 ns
T_C	200 μ s

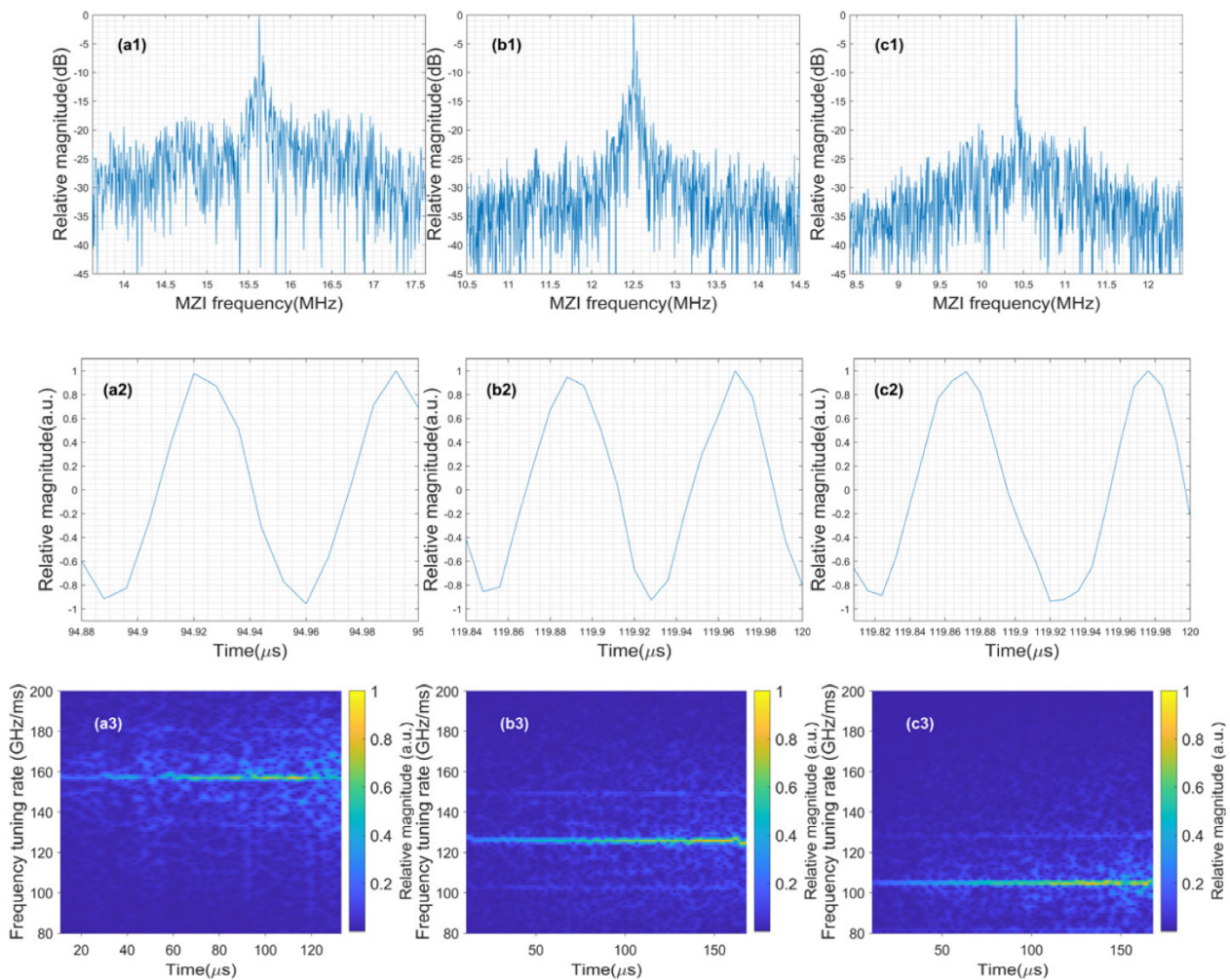


Figure 4. Experimental results with the various time delays and optical frequency tuning rates. (a1–a3) Tuning rate, 10 ns; (b1–b3) time delay, 100 ns; (c1–c3) time delay, 250 ns; (a1–c1) FFT results of the MZI signals in the region of interest (ROI) in the frequency domain; (a2–c2) results of the MZI signals in the time domain with two periods; (a3–c3) short-time FFT (STFFT) results of the MZI signals with the Hamming window.

Therefore, it can be safely concluded that only when a short time delay and low-optical-frequency tuning velocity are utilized in the controlling system can an SCL with limited optical bandwidth generate the highly linear optical source to capture the ideal measurements.

4. Conclusions

In summary, this work demonstrates and experimentally evaluates an OFDR fiber sensing system that can directly simulate and judge the stability of semiconductor lasers for

sensing applications, and such a module has been proved by various parameters. Generally, since the core of the OFDR system is the constant tuning rate of the SCL, the optical error plays a significant role when precise results are required. Thus, a detailed error module would inspire the research direction of prior OFDR systems used for sensing and further broaden their application in other areas, including optical sensors, laser spectroscopy, and SCL performance characterization.

Funding: This work was supported by the National Natural Science Foundation of China (No. 62105152, 62175111); the Key Research and Development programs in Jiangsu China (Grant no. BE2018126); the Fundamental Research Funds for the Central Universities (Grant no. 30919011401, 30920010001, JSGP202202, 30922010715, 30922010718); and the Leading Technology of Jiangsu Basic Research Plan (Grant no. BK20192003).

Institutional Review Board Statement: Not applicable.

Informed Consent Statement: Not applicable.

Data Availability Statement: Not applicable.

Conflicts of Interest: The authors declare no conflict of interest.

List of the Symbols and Abbreviations

Symbol/Abbreviation	Meaning
SCL	Semiconductor laser
MZI	Mach-Zender Interferometer
CPL	Optical coupler
BPD	Balanced photodetector
CL	Laser frequency-sweep control loop
f_s	System sampling rate
τ_d	MZI delay time
T_C	Controlling period
f_0	Initial optical frequency
v_0	Optical tuning rate
$e(t)$	Optical frequency error
B	Optical bandwidth

References

- Lee, B. Review of the present status of optical fiber sensors. *Opt. Fiber Technol.* **2003**, *9*, 57–79. [[CrossRef](#)]
- Pan, J.; Guan, K.; Qiu, X.; Wang, W.; Zhang, M.; Jiang, J.; Zhang, E.; Zhou, F.Q. Advantages of low-cost, miniature, intelligent EDFAs for next-generation dynamic metro/access networks. *Opt. Fiber Technol.* **2003**, *9*, 80–94. [[CrossRef](#)]
- Yao, Z.; Mauldin, T.; Xu, Z.; Hefferman, G.; Wei, T. Compact multifunction digital OFDR system without using an auxiliary interferometer. *Appl. Opt.* **2021**, *60*, 7523–7529. [[CrossRef](#)] [[PubMed](#)]
- Yao, Z.; Wei, T.; Hefferman, G.; Ren, K. Real-time signal processing for sub-THz range grating-based distributed fiber sensing. *Rev. Sci. Instrum.* **2018**, *89*, 085005. [[CrossRef](#)] [[PubMed](#)]
- Holzwarth, R.; Udem, T.; Hänsch, T.W.; Knight, J.; Wadsworth, W.; Russell, P.S.J. Optical frequency synthesizer for precision spectroscopy. *Phys. Rev. Lett.* **2000**, *85*, 2264. [[CrossRef](#)]
- Yao, Z.; Mauldin, T.; Xu, Z.; Hefferman, G.; Wei, T. Breaking limitations of fiber identification in traditional OFDR systems via compensation of initial optical frequency instability. *Opt. Lett.* **2020**, *45*, 6086–6089. [[CrossRef](#)]
- Du, Y.; Jothibas, S.; Zhuang, Y.; Zhu, C.; Huang, J. Unclonable Optical Fiber Identification Based on Rayleigh Backscattering Signatures. *J. Light. Technol.* **2017**, *35*, 4634–4640. [[CrossRef](#)]
- Lu, P.; Lalam, N.; Badar, M.; Liu, B.; Chorpening, B.T.; Buric, M.P.; Ohodnicki, P.R. Distributed optical fiber sensing: Review and perspective. *Appl. Phys. Rev.* **2019**, *6*, 041302. [[CrossRef](#)]
- Zhu, Z.; Liu, L.; Liu, Z.; Zhang, Y.; Zhang, Y. Surface-plasmon-resonance-based optical-fiber temperature sensor with high sensitivity and high figure of merit. *Opt. Lett.* **2017**, *42*, 2948–2951. [[CrossRef](#)]
- DiLazaro, T.; Nehmetallah, G. Large-volume, low-cost, high-precision FMCW tomography using stitched DFBs. *Opt. Express.* **2018**, *26*, 2891–2904. [[CrossRef](#)]
- Xie, W.; Zhou, Q.; Bretenaker, F.; Xia, Z.; Shi, H.; Qin, J.; Dong, Y.; Hu, W. Fourier transform-limited optical frequency-modulated continuous-wave interferometry over several tens of laser coherence lengths. *Opt. Lett.* **2016**, *41*, 2962–2965. [[CrossRef](#)] [[PubMed](#)]

12. Yao, Z.; Mauldin, T.; Hefferman, G.M.; Wei, T. Digitally integrated self-trained pre-distortion curve finder for passive sweep linearization of semiconductor lasers. *IEEE J. Sel. Top. Quantum Electron.* **2019**, *25*, 1–5.
13. Colautti, M.; Piccioli, F.S.; Ristanovic, Z.; Lombardi, P.; Moradi, A.; Adhikari, S.; Deperasinska, I.; Kozankiewicz, B.; Orrit, M.; Toninelli, C. Laser-induced frequency tuning of Fourier-limited single-molecule emitters. *ACS Nano* **2020**, *14*, 13584–13592. [[CrossRef](#)] [[PubMed](#)]
14. Wang, J.; Haldar, M.; Li, L.; Mendis, F. Enhancement of modulation bandwidth of laser diodes by injection locking. *IEEE Photonics Technol. Lett.* **1996**, *8*, 34–36. [[CrossRef](#)]
15. Martin, A.; Dodane, D.; Leviandier, L.; Dolfi, D.; Naughton, A.; O'Brien, P.; Spuessens, T.; Baets, R.; Lepage, G.; Verheyen, P. Photonic integrated circuit-based FMCW coherent LiDAR. *J. Light. Technol.* **2018**, *36*, 4640–4645. [[CrossRef](#)]
16. Huang, D.; Tran, M.A.; Guo, J.; Peters, J.; Komljenovic, T.; Malik, A.; Morton, P.A.; Bowers, J.E. High-power sub-kHz linewidth lasers fully integrated on silicon. *Optica* **2019**, *6*, 745–752. [[CrossRef](#)]
17. Riemensberger, J.; Lukashchuk, A.; Karpov, M.; Weng, W.; Lucas, E.; Liu, J.; Kippenberg, T.J. Massively parallel coherent laser ranging using a soliton microcomb. *Nature* **2020**, *581*, 164–170. [[CrossRef](#)]
18. Dai, J.; Karpowicz, N.; Zhang, X.C. Coherent Polarization Control of Terahertz Waves Generated from Two-Color Laser-Induced Gas Plasma. *Phys. Rev. Lett.* **2009**, *103*, 23001. [[CrossRef](#)]
19. Henry, C. Phase noise in semiconductor lasers. *J. Light. Technol.* **1986**, *4*, 298–311. [[CrossRef](#)]
20. Huynh, T.N.; Dúill, S.P.Ó.; Nguyen, L.; Rusch, L.A.; Barry, L.P. Simple analytical model for low-frequency frequency-modulation noise of monolithic tunable lasers. *Appl. Opt.* **2014**, *53*, 830–835. [[CrossRef](#)]
21. Yao, Z.; Mauldin, T.; Xu, Z.; Hefferman, G.; Wei, T. An integrated OFDR system using combined swept-laser linearization and phase error compensation. *IEEE Trans. Instrum. Meas.* **2020**, *70*, 1–8. [[CrossRef](#)]
22. Zhao, E.; Shen, H.; Liu, S.; Liu, G.; Zhou, B.; Wang, C.; Xing, C.; Miao, P.; Shi, Y. Auxiliary interferometer in an optoelectronic swept-frequency laser and its application to the measurement of the group refractive index. *Appl. Opt.* **2020**, *59*, 10294–10303. [[CrossRef](#)]
23. Guo, R.; Lu, J.; Liu, S.; Shi, Y.; Zhou, Y.; Chen, Y.; Luan, J.; Chen, X. Multisection DFB tunable laser based on REC technique and tuning by injection current. *IEEE Photonics J.* **2016**, *8*, 1–7. [[CrossRef](#)]
24. Karlsson, C.J.; Olsson, F.Å. Linearization of the frequency sweep of a frequency-modulated continuous-wave semiconductor laser radar and the resulting ranging performance. *Appl. Opt.* **1999**, *38*, 3376–3386. [[CrossRef](#)]
25. Yao, Z.; Xu, Z.; Mauldin, T.; Hefferman, G.; Wei, T. A reconfigurable architecture for continuous double-sided swept-laser linearization. *J. Light. Technol.* **2020**, *38*, 5170–5176. [[CrossRef](#)]
26. Yao, Z.; Mauldin, T.; Hefferman, G.; Xu, Z.; Liu, M.; Wei, T. Low-cost optical fiber physical unclonable function reader based on a digitally integrated semiconductor LiDAR. *Appl. Opt.* **2019**, *58*, 6211–6216. [[CrossRef](#)]
27. Delprat, N.; Escudié, B.; Guillemain, P.; Kronland-Martinet, R.; Tchamitchian, P.; Torresani, B. Asymptotic wavelet and Gabor analysis: Extraction of instantaneous frequencies. *IEEE Trans. Inf. Theory* **1992**, *38*, 644–664. [[CrossRef](#)]
28. Urick, V.J.; Bucholtz, F.; Devgan, P.S.; McKinney, J.D.; Williams, K.J. Phase modulation with interferometric detection as an alternative to intensity modulation with direct detection for analog-photonic links. *IEEE Trans. Microw. Theory Tech.* **2007**, *55*, 1978–1985. [[CrossRef](#)]
29. Kay, S.M. Fundamentals of statistical signal processing: Estimation theory. *Technometrics* **1993**, *37*, 465.
30. Xu, Z.; Mauldin, T.; Yao, Z.; Pei, S.; Wei, T.; Yang, Q. A Bus Authentication and Anti-Probing Architecture Extending Hardware Trusted Computing Base Off CPU Chips and Beyond. In Proceedings of the 2020 ACM/IEEE 47th Annual International Symposium on Computer Architecture (ISCA), Valencia, Spain, 30 May–3 June 2020; pp. 749–761.